IEEE Access
Multidisciplinary | Rapid Review | Open Access Journal

Received February 14, 2019, accepted February 26, 2019, date of publication March 1, 2019, date of current version March 20, 2019.

Digital Object Identifier 10.1109/ACCESS.2019.2902445

Compressed Sensing Radar Imaging With Magnitude Sparse Representation

JUNGANG YANG, (Member, IEEE), TIAN JIN, (Member, IEEE), AND XIAOTAO HUANG, (Member, IEEE)

College of Electronic Science and Technology, National University of Defense Technology, Changsha 410073, China

Corresponding author: Tian Jin (tianjin@nudt.edu.cn)

This work was supported in part by the National Natural Science Foundation of China under Grant 61401474, and in part by the Hunan Provincial Natural Science Foundation under Grant 2016JJ3025.

ABSTRACT Compressed sensing (CS) is a sparsity-driven and regularization-based approach. The CS theory has led to superior imaging methods, offering a number of benefits, including increased image quality and robustness to the limitations in data quantity. In such imaging methods, if the targets are not originally sparse (not sparse in the canonical basis), sparse representation is required. However, in synthetic aperture radar (SAR) imaging scenarios, owing to the potentially random phase of the scene, it is very difficult to find bases to sparsify a complex-valued and extended scene. In this paper, an improved framework to handle the magnitude and phase of the scene separately is proposed. Although the phase of the scene is potentially random, the magnitude can usually be sparsely represented. In the proposed framework, besides the sparsity, the real-valued information of the magnitude and the coefficient distribution of the sparse representation are also utilized. In the reconstruction process, the magnitude of the scene is constrained to be real-valued, and the coefficients of the sparse representation are limited in the low-frequency area. A novel gradient-based optimization algorithm is developed to solve the proposed framework effectively. Since more *a priori* knowledge is utilized in the proposed algorithm, it can reduce the computational complexity and improve the reconstruction precision. The simulation results and real data results from an airborne SAR system are presented to show the superiority of the proposed algorithm.

INDEX TERMS Radar imaging, regularization-based reconstruction, magnitude sparse representation, compressed sensing (CS).

I. INTRODUCTION

Traditional radar imaging methods are mostly based on matched filtering [1]. These methods require signals to be sampled at or above the Nyquist rate. In practice, acquiring the signal at the Nyquist rate might be time-consuming, expensive, or inefficient. In addition, the resolution of traditional radar imaging methods is limited by the signal bandwidth. Recently, the sparsity properties of targets have attracted much interest in radar imaging. In radar imaging applications, the sparsity property can be satisfied if there are only a few dominant scattering centers in the scene or on the target. This is often true especially for targets like vehicles, airplanes and so on [2]. Another case where sparsity can hold is that the scene is not originally sparse, but can be represented by a set of bases with sparse coefficients (i.e. a sparse representation or a sparsifying transform). Sparsity-driven and regularization-based approaches have led to superior imaging algorithms offering a number of benefits, including increased image quality and robustness to limitations in data quantity [3]–[6]. A special case of sparsity-driven and regularization-based methods is compressed sensing (CS) [7]–[12], which is used to reduce the number of collected samples.

Many regularization-based or CS-based algorithms have been proposed for radar imaging [2], [13]–[15], including synthetic aperture radar (SAR) imaging [16]–[20], SAR ground moving target indication (SAR/GMTI) [21]–[25], tomography SAR [26]–[31] and 3D SAR imaging [32]–[34], inverse SAR (ISAR) [35]–[37], and ground penetrating radar (GPR) [38]–[40].

In SAR imaging scenarios, except for the case of a few dominant scatterers in a low reflective surrounding, extended scenes are usually not originally sparse (not sparse in the

The associate editor coordinating the review of this manuscript and approving it for publication was Chenhao Qi.

canonical basis) [2]. In this case, if we want to use sparsity-driven methods, sparse representation is needed.

Sparse representation has successfully been used in CS-based optical imaging [41]. In such a scenario, sparse representation is performed on real-valued images, and many conventional bases are effective. As a well known fact, optical images usually can be transformed into a few dominant coefficients using wavelets, the discrete Fourier transform or the discrete cosine transform (DCT).

However, one aspect of SAR that differentiates it from incoherent imaging scenarios is that both the observed data and the reconstructed images involve complex-valued quantities. Owing to the potentially random phase of the scene in SAR, it is very difficult to find bases to sparsify a complex-valued and extended scene [42], [43]. Although many interesting ideas are presented for sparsity-driven or CS-based SAR imaging, most of them are only demonstrated by simulation or for real data with a few dominant scatterers. Only a very few papers investigated real data for extended scenes.

Instead of considering sparsity issues for a complex-valued scene, another idea is to handle the magnitude and phase separately. Although the phase of the scene is potentially random, the magnitude of the scene can usually be sparsely represented. Samadi *et al.* [44] proposed an approach to utilize the sparsity information in the magnitude of the complex-valued scene in SAR imaging. The superiority of the algorithm lies in high quality of final images and its robustness to limited data. The algorithm proposed in [44] uses an iterative approach to estimate the magnitude and the phase of the scene separately. Since the calculations of both magnitude and phase estimation are non-linear and complex, the computation complexity is large for a single iteration. Considering a number of iterations are needed in order to converge to a good result, the algorithm proposed in [44] is very time consuming.

In this paper, an improved magnitude sparse representation method for compressed sensing SAR imaging is proposed. Besides the sparsity of the magnitude of the scene, further characteristics of the magnitude of the scene are utilized in our algorithm.

It is well known that optical images will concentrated at low frequencies if we perform a Fourier transform or DCT. Similar to optical images, in many situations, the magnitude of a SAR scene will not only be sparse, but also be concentrated at low frequencies. So, we can utilize this characteristic in sparse representation. We will use only the bases corresponding to the low frequency components to represent the magnitude, instead of using the complete bases. In this way, the size of the problem can be reduced and the computational complexity can be consequently reduced.

Besides the coefficient distribution of the sparse representation, we also utilize the real-valued information of the magnitude in the proposed algorithm. The algorithm in [44] does not constrain the magnitude to be real-valued in the reconstruction process. In our algorithm, this information is utilized as an additional constraint in the reconstruction process.

The algorithm proposed in this paper has the following superiorities:

1. Since the number of bases is reduced, the size of the sparse representation matrix is also reduced. So the computational complexity can be consequently reduced.

2. Since more a priori knowledge is utilized, the reconstruction precision can be improved and the quality of the produced image can be increased.

These two points are demonstrated by simulation results and real data results from an airborne SAR system.

This paper is organized as follows: in Section II, the SAR imaging model is described along with the geometry and signal equations. In Section III, magnitude sparsity-driven method is introduced. In Section IV, the improved method is proposed, including issues about utilizing the real-valued information of the magnitude, reduced bases for sparse representation, structure of two-dimensional (2D) sparse representation, flowchart and solution of the proposed algorithm, computational complexity and parameter analysis. In Section V, simulation and real data results are presented to show the advantages of the proposed algorithm. Finally, in Section VI, conclusions for this paper are drawn.

II. SAR IMAGING MODEL

Consider the transmitted signal of the radar is

$$s_t(t_r) = p(t_r)\exp(j2\pi f_c t_r) \tag{1}$$

where t_r is the fast time (signal time) [1], $p(t_r)$ is the transmitted waveform and f_c is the carrier frequency. We assume that a typical linear frequency modulated (LFM) waveform is used, then $p(t_r)$ is given by

$$p(t_r) = \mathrm{rect}(t_r/T_p)\exp(j\pi\gamma t_r^2) \tag{2}$$

where $\mathrm{rect}(\cdot)$ is the time window, which is a rectangular function, T_p is the pulse duration and γ is the chirp rate.

Now suppose the transmitted signal is reflected by a point scatterer at range R, the demodulated echo is

$$s(t_r) = g \cdot p(t_r - 2R/c)\exp(-j4\pi f_c R/c) \tag{3}$$

where g is the reflectivity coefficient of the target and c is the velocity of light.

In the case of SAR imaging, the radar transmits a pulse train while it is in motion. The range of the target changes with respect to the slow time (azimuth time). In addition, the received signal is the superposition of the echo from the whole illuminated scene. So the 2D SAR data can be written as

$$s(t_a, t_r) = \iint_D g(x, y) \cdot p(t_r - 2R(t_a, x, y)/c) \cdot \exp(-j4\pi f_c R(t_a, x, y)/c)dxdy \tag{4}$$

where t_a is the azimuth time, D denotes the illuminated area, x and y are the coordinates of the target, $g(x, y)$ is the reflectivity coefficient of the target at position (x, y) and $R(t_a, x, y)$

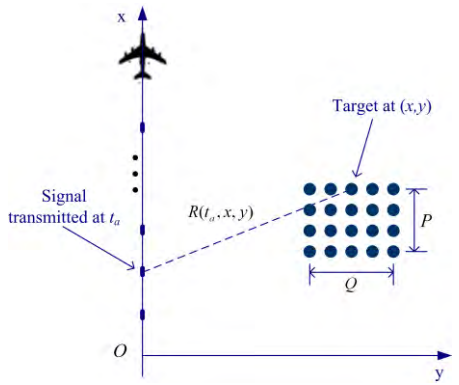

FIGURE 1. SAR imaging model.

is the range of the target at (x, y) when the radar is at azimuth time t_a.

In practice, the fast time and the slow time will be discrete due to the sampling process. The scene is also discretized into a grid format in order to use regularization-based methods. The geometry and signal model is illustrated in Fig. 1, where P is the number of points along the x axis and Q is the number of points along the y axis after the discretization of the scene.

In order to use the regularization-based reconstruction approach conveniently, the SAR signal should be rewritten as matrix form as [45]

$$\mathbf{s} = \mathbf{A}\mathbf{g} \tag{5}$$

where $\mathbf{s}$ is a $MN \times 1$ vector, which is formed by stacking the samples of $s(t_a, t_r)$ in (4). $\mathbf{A}$ is a $MN \times PQ$ matrix, the elements of which are the values corresponding to $p(t_r - 2R(t_a, x, y)/c) \cdot \exp(-j4\pi f_c R(t_a, x, y)/c)$ in (4). $\mathbf{g}$ is a $PQ \times 1$ vector, which is formed by stacking the discretized $g(x, y)$ in (4).

III. MAGNITUDE SPARSITY-DRIVEN RECONSTRUCTION FOR SAR

Let us briefly review the traditional radar imaging method first. Using the measurement model expressed in (5), the traditional imaging algorithm based on matched filtering can be written as

$$\hat{\mathbf{g}} = \mathbf{A}^H \mathbf{s} \tag{6}$$

where $(\cdot)^H$ denotes the Hermitian of a matrix.

Equation (6) corresponds to the traditional backprojection imaging algorithm in SAR. All the other traditional imaging algorithms based on matched filtering, such as range Doppler (RD), chirp scaling (CS), Omega-K and fast backprojection, are variants and approximations of (6). The aim of these algorithms is to reduce the computational cost in practical application.

The matched filtering algorithms require the signals to be sampled above the Nyquist rate and the resolution is limited by the signal bandwidth. No *a priori* knowledge of the scene is utilized in these algorithms. Recently, sparsity has attracted many interests in radar imaging. Sparsity-driven and regularization-based approaches have led to superior imaging algorithms [3].

Now, let us briefly review conventional sparsity-driven or CS-based imaging algorithms in SAR. Such algorithms assume that the scene is originally sparse, so the scene (i.e. $\mathbf{g}$ in equation (5)) can be obtained by a sparse reconstruction as

$$\min_{\mathbf{g}} \|\mathbf{g}\|_1 \quad \text{s.t. } \mathbf{s} = \mathbf{A}\mathbf{g} \tag{7}$$

where $\|\cdot\|_1$ denotes the ℓ_1-norm. Equation (7) can be solved by basis pursuit [46] or matched pursuit [47] algorithms. In the following simulation and real data processing in this paper, we use the spectral projected gradient for L1 minimization (SPGL1) [48] to solve (7).

In the case of that the scene is not originally sparse, equation (7) is no longer valid and a sparse representation is needed. As mentioned in the introduction, since the phase of the scene is potentially random, it is difficult to find bases to sparsify $\mathbf{g}$. Since we are usually interested in the magnitude of a SAR image, a feasible idea is to handle the magnitude and phase separately. Although the phase of the scene is potentially random, the magnitude of the scene can usually be sparsely represented [44]. We denote the scene with magnitude and phase separately as

$$\mathbf{g} = \mathbf{P}\,|\mathbf{g}| \tag{8}$$

where $\mathbf{P} = \text{diag}\{\exp[j\boldsymbol{\phi}(\mathbf{g})]\}$ is a diagonal matrix, $\boldsymbol{\phi}(\mathbf{g})$ are the phases of $\mathbf{g}$, and $|\mathbf{g}|$ is the magnitude of the scene $\mathbf{g}$. We consider that the magnitude can be sparsely represented as

$$|\mathbf{g}| = \boldsymbol{\Phi}\boldsymbol{\alpha} \tag{9}$$

where $\boldsymbol{\Phi}$ contains the bases and α is the sparse coefficients.

By denoting $\mathbf{g}$ with magnitude and phase, the SAR measurement model in (5) can be rewritten as

$$\mathbf{s} = \mathbf{A}\mathbf{g} = \mathbf{A}\mathbf{P}\,|\mathbf{g}| = \mathbf{A}\mathbf{P}\boldsymbol{\Phi}\boldsymbol{\alpha} \tag{10}$$

In (10), if we know $\mathbf{P}$, the sparse coefficients α can be obtained using standard sparse reconstruction algorithms such as basis pursuit [46] or matched pursuit [47]. However, the difficulty is that we do not know $\mathbf{P}$ (i.e. the phase of the scene). Using the algorithm proposed in [44], this problem can be solved by the following iterative approach:

The details to solve step 1 and step 2 in Algorithm 1 are shown in [44]. Although the magnitude sparsity-driven algorithm summarized in Algorithm 1 is an effective way to solve the random phase problem, it also has some limitations. In this algorithm, the number of the unknown phase terms for the scene is equal to the number of grid points. The magnitude is represented by a set of sparse coefficients, but the positions of the dominant coefficients are totally unknown. These mean that the degree of freedom for the unknown variables is high. The real-valued property of the image magnitude is also unused. This is not beneficial for reconstruction. In the

Algorithm 1 Magnitude Sparsity-Driven Reconstruction [44]

Initialize: Start with an initial estimate of $\mathbf{g}$ that could be its traditional matched filtering result. Then initial estimates of $\mathbf{P}$ and $\boldsymbol{\alpha}$ are also obtained.

Step 1: Using the estimate of $\mathbf{P}$, solve for $\boldsymbol{\alpha}$ as

$$\min_{\boldsymbol{\alpha}} \|\boldsymbol{\alpha}\|_1 \quad \text{s.t. } \mathbf{s} = \mathbf{AP}\boldsymbol{\Phi}\boldsymbol{\alpha} \tag{11}$$

Step 2: Using the new estimate of $\boldsymbol{\alpha}$, a new estimate of $\mathbf{P}$ can be obtained as

$$\min_{\boldsymbol{\beta}} \|\mathbf{s} - \mathbf{AB}\boldsymbol{\beta}\|_2 \quad \text{s.t. } |\boldsymbol{\beta}| = \mathbf{1} \tag{12}$$

where $\mathbf{B} = \text{diag}\{|\mathbf{g}|\}$, $\boldsymbol{\beta}$ is a vector formed by stacking the diagonal elements of $\mathbf{P}$, and $\mathbf{1}$ is a $PQ \times 1$ vector with all elements are equal to 1.

Step 3: Update $\mathbf{P}$ using the new estimate result of step 2 and return to step 1.

Terminate when the change of $\boldsymbol{\alpha}$ or $\boldsymbol{\beta}$ is less than a predetermined threshold.

following section, we will exploit more *a priori* knowledge to improve Algorithm 1.

IV. PROPOSED MAGNITUDE SPARSE REPRESENTATION METHOD

The above section introduced the magnitude sparsity-driven reconstruction for SAR imaging. In this section, we will exploit more *a priori* knowledge of the scene to improve the existing algorithm. We will utilize the real-valued information of the magnitude and the coefficient distribution of the sparse representation.

A. UTILIZING THE REAL-VALUED INFORMATION OF THE MAGNITUDE

In (11), $\boldsymbol{\Phi}\boldsymbol{\alpha} = |\mathbf{g}|$ should be real-valued. However, this knowledge is not exploited in Algorithm 1. There is no constraint to force $\boldsymbol{\Phi}\boldsymbol{\alpha}$ to be real-valued. In the algorithm proposed in this paper, we will utilize this information. If we choose proper bases, such as the DCT, it can represent a real-valued signal with real-valued coefficients. That is to say, if we use the DCT bases, real-valued coefficients $\boldsymbol{\alpha}$ will be equivalent to real-valued magnitudes $\boldsymbol{\Phi}\boldsymbol{\alpha}$. So, we just need to constrain $\boldsymbol{\alpha}$ to be real-valued in order to obtain a real-valued magnitude. This can be realized by adding a constraint to the optimization problem in (11). Thus equation (11) is modified to

$$\min_{\boldsymbol{\alpha}} \|\boldsymbol{\alpha}\|_1 \quad \text{s.t. } \mathbf{s} = \mathbf{AP}\boldsymbol{\Phi}\boldsymbol{\alpha} \text{ and } \boldsymbol{\alpha} = \boldsymbol{\alpha}^* \tag{13}$$

where $\boldsymbol{\Phi}$ contains the DCT bases and $\boldsymbol{\alpha}^*$ denotes the conjugation of $\boldsymbol{\alpha}$.

In this way, the real-valued information of the magnitude is utilized, and the reconstruction will be improved. We will demonstrate this in Section V with both simulation and real data results.

B. REDUCED BASES FOR SPARSE REPRESENTATION

Let us consider the sparse representation for the magnitude again. In fact, similar to optical images, if we perform the DCT on the magnitude of a SAR image, the coefficients are usually concentrated at low frequencies. We will utilize this *a priori* knowledge in our algorithm. It means that the non-zero or dominant coefficients will be located at low frequencies. The coefficients corresponding to high frequency bases will be zero or very small, so they can be excluded in the sparse representation matrix. Consequently, the size of the optimization problem can be reduced.

Let us focus on the sparse representation matrix $\boldsymbol{\Phi}$ in equation (9). $\boldsymbol{\Phi}$ contains the bases to represent $|\mathbf{g}|$; conventionally, these bases are complete and orthogonal. So the number of bases is equal to the signal dimension and $\boldsymbol{\Phi}$ is a square matrix ($PQ \times PQ$). As mentioned above, if we use only the low frequency bases, the number of columns of $\boldsymbol{\Phi}$ can be reduced, so that the dimensions of $\boldsymbol{\alpha}$ and the optimization problem can be reduced accordingly, while the precision is nearly the same. Let $\boldsymbol{\Phi}'$ denote the matrix of the reduced bases. Then the size of $\boldsymbol{\Phi}'$ is $PQ \times K$, where K is the number of low frequency bases, which can be significantly smaller than PQ. Then the sparse representation shown in (9) can be modified to

$$|\mathbf{g}| = \boldsymbol{\Phi}'\boldsymbol{\alpha}' \tag{14}$$

The size of $\boldsymbol{\alpha}'$ is $K \times 1$, which can be significantly smaller than the size of $\boldsymbol{\alpha}$. For example, assuming that half bases are used for representation both in columns and rows, $K = PQ/4$.

The needed number of bases for sparse representation depends on the characteristic of the scene. The value of the number of bases can be experientially determined according to the statistic result of many scenes, and it also can be adjusted according to different type of scenes.

Using the reduced bases for sparse representation, the size of the optimization problem (13) is consequently reduced. So the computational complexity will also be reduced. We will analyze this reduction in subsection E of this section.

C. STRUCTURE OF 2D SPARSE REPRESENTATION WITH REDUCED BASES

As SAR is a 2D imaging system, in this subsection, we will consider the structure of the sparse representation for the 2D scene. The sparsity-driven and regularization-based model is usually expressed in matrix form. In order to analyze the sparse representation in combination with the regularization model conveniently, we should write it in a matrix form too. We begin with the sparse representation for the magnitude of the 2D reflectivity map. The sparse representation can be applied both to the columns and rows of the 2D map, and it can be expressed as

$$|\mathbf{G}| = \boldsymbol{\Phi}_c \mathbf{X} \boldsymbol{\Phi}_r \tag{15}$$

where $|\mathbf{G}|$ is the 2D reflectivity map, which is the original form of $|\mathbf{g}|$. $\mathbf{X}$ is the 2D sparse coefficients, which is the

original form of $\boldsymbol{\alpha}$ or $\boldsymbol{\alpha}'$. $\boldsymbol{\Phi}_c$ are the bases for the columns and $\boldsymbol{\Phi}_r$ are the bases for the rows. Assuming that the reduced bases are used, the size of $\boldsymbol{\Phi}_c$ is $P \times K_1$ and the size of $\boldsymbol{\Phi}_r$ is $K_2 \times Q$, where K_1 and K_2 are the number of bases used for column and row representation respectively. The size of $\mathbf{X}$ is $K_1 \times K_2$.

As shown in Section II, in order to express the equations in matrix form, the 2D reflectivity map $|\mathbf{G}|$ is stacked into a column vector $|\mathbf{g}|$. The 2D coefficients $\mathbf{X}$ are also stacked into the column vector $\boldsymbol{\alpha}'$. Therefore, the sparse representation in (15) should also be reformatted accordingly. The sparse representation for the columns should be reformatted as

$$\tilde{\boldsymbol{\Phi}}_c = \begin{bmatrix} \boldsymbol{\Phi}_c & & & \\ & \boldsymbol{\Phi}_c & & \\ & & \ddots & \\ & & & \boldsymbol{\Phi}_c \end{bmatrix} \tag{16}$$

where $\tilde{\boldsymbol{\Phi}}_c$ is a $PQ \times K_1 Q$ matrix. Let

$$\begin{aligned} &\boldsymbol{\varphi}_{rij} \\ &= \Big[\underbrace{0}_{(j-1)zeros} \quad \phi_r(1,i) \quad \underbrace{0}_{(K_1-1)zeros} \quad \phi_r(2,i) \cdots \phi_r(K_2,i) \quad \underbrace{0}_{(K_1-j)zeros} \Big] \\ &i = 1, 2, \cdots, Q \\ &j = 1, 2, \cdots, K_1. \end{aligned} \tag{17}$$

where $\varphi_r(\cdot)$ denotes the elements of $\boldsymbol{\Phi}_r$.

$$\boldsymbol{\Phi}_{ri} = \begin{bmatrix} \boldsymbol{\Phi}_{ri1} \\ \boldsymbol{\Phi}_{ri2} \\ \vdots \\ \boldsymbol{\Phi}_{riK_1} \end{bmatrix} \tag{18}$$

The sparse representation for the rows should be reformatted as

$$\tilde{\boldsymbol{\Phi}}_r = \begin{bmatrix} \boldsymbol{\Phi}_{r1} \\ \boldsymbol{\Phi}_{r2} \\ \vdots \\ \boldsymbol{\Phi}_{rQ} \end{bmatrix} \tag{19}$$

where $\tilde{\boldsymbol{\Phi}}_r$ is a $K_1 Q \times K_1 K_2$ matrix.

Then the sparse representation for $|\mathbf{g}|$ is

$$|\mathbf{g}| = \tilde{\boldsymbol{\Phi}}_c \tilde{\boldsymbol{\Phi}}_r \boldsymbol{\alpha}' = \boldsymbol{\Phi}' \boldsymbol{\alpha}' \tag{20}$$

where $\boldsymbol{\Phi}' = \tilde{\boldsymbol{\Phi}}_c \tilde{\boldsymbol{\Phi}}_r$, the size of $\boldsymbol{\Phi}'$ is $PQ \times K_1 K_2$ and the size of $\boldsymbol{\alpha}'$ is $K_1 K_2 \times 1$. Note that the previously mentioned K is equal to $K_1 K_2$ here.

D. FLOWCHART AND SOLUTION OF THE PROPOSED ALGORITHM

Combining subsection *A* and *B*, the flowchart of the proposed algorithm can be summarized as follows:

Now, let us consider how to solve step 1 and step 2 in Algorithm 2. To solve step 1 in Algorithm 2, the constrained

Algorithm 2 Proposed Algorithm

Initialize: Choose proper bases which can sparsely represent the real-valued magnitude with real-valued coefficients. Only use its reduced form $\boldsymbol{\Phi}'$ for representation. Start with an initial estimate of $\mathbf{g}$ that could be its traditional matched filtering result. Then the initial estimate of $\mathbf{P}$ and $\boldsymbol{\alpha}'$ are also obtained.

Step 1: Using the estimate of $\mathbf{P}$, solve for $\boldsymbol{\alpha}'$ as

$$\min_{\boldsymbol{\alpha}'} \left\| \boldsymbol{\alpha}' \right\|_1 \quad \text{s.t. } \mathbf{s} = \mathbf{A}\mathbf{P}\boldsymbol{\Phi}'\boldsymbol{\alpha}' \text{ and } \boldsymbol{\alpha}' = \boldsymbol{\alpha}'^{*} \tag{21}$$

Step 2: Using the new estimate of $\boldsymbol{\alpha}'$, a new estimate of $\mathbf{P}$ can be obtained as

$$\min_{\boldsymbol{\beta}} \|\mathbf{s} - \mathbf{A}\mathbf{B}\boldsymbol{\beta}\|_2 \quad \text{s.t. } |\boldsymbol{\beta}| = \mathbf{1} \tag{22}$$

where $\mathbf{B} = \text{diag}\{|\mathbf{g}|\}$ and $\boldsymbol{\beta}$ is a vector formed by stacking the diagonal elements of $\mathbf{P}$.

Step 3: Update $\mathbf{P}$ using the new estimate result of step 2 and return to step 1.

Terminate when the change of $\boldsymbol{\alpha}'$ or $\boldsymbol{\beta}$ is less than a predetermined threshold.

optimization problem (21) can be replaced with the following unconstrained problem

$$\min_{\boldsymbol{\alpha}'} \left\| \boldsymbol{\alpha}' \right\|_1 + \lambda_1 \left\| \mathbf{s} - \mathbf{A}\mathbf{P}\boldsymbol{\Phi}'\boldsymbol{\alpha}' \right\|_2^2 + \lambda_2 \left\| \boldsymbol{\alpha}' - \boldsymbol{\alpha}'^{*} \right\|_2^2 \tag{23}$$

where λ_1 and λ_2 are the regularization parameters. Equation (23) can be solved using gradient-based algorithms such as quasi-Newton. To use gradient-based algorithms, the gradient of the cost function should be provided to the algorithm. We have

$$\begin{aligned} \nabla\boldsymbol{\alpha}' = \phi(\boldsymbol{\alpha}') &+ 2\lambda_1(\mathbf{A}\mathbf{P}\boldsymbol{\Phi}')^H(\mathbf{A}\mathbf{P}\boldsymbol{\Phi}')\boldsymbol{\alpha}' \\ &-2\lambda_1(\mathbf{A}\mathbf{P}\boldsymbol{\Phi}')^H\mathbf{s} + 2\lambda_2(\boldsymbol{\alpha}' - \boldsymbol{\alpha}'^{*}) \end{aligned} \tag{24}$$

where $\phi(\boldsymbol{\alpha}') = \exp\left[j\varphi(\boldsymbol{\alpha}')\right]$, $\varphi(\boldsymbol{\alpha}')$ is the phase of $\boldsymbol{\alpha}'$ and $\boldsymbol{\alpha}'^{*}$ is the conjugation of $\boldsymbol{\alpha}'$.

In quasi-Newton algorithms, besides the gradient, another important issue is how to determine the Hessian matrix. As mentioned in [3], standard quasi-Newton algorithms with a conventional Hessian update scheme perform poorly for non-quadratic problems. Here we will derive a novel Hessian matrix, which has been proved to be effective by simulation and real data. The gradient expression in (24) can be rewritten as

$$\nabla\boldsymbol{\alpha}' = \mathbf{H}(\boldsymbol{\alpha}')\boldsymbol{\alpha}' - 2\lambda_1(\mathbf{A}\mathbf{P}\Phi')^H\mathbf{s} \tag{25}$$

where

$$\mathbf{H}(\boldsymbol{\alpha}') = \boldsymbol{\Psi}(\boldsymbol{\alpha}') + 2\lambda_1(\mathbf{A}\mathbf{P}\boldsymbol{\Phi}')^H(\mathbf{A}\mathbf{P}\boldsymbol{\Phi}') + 2\lambda_2\mathbf{I} - 2\lambda_2\phi(\boldsymbol{\alpha}')^{-2} \tag{26}$$

$$\boldsymbol{\Psi}(\boldsymbol{\alpha}') = \text{diag}\left\{1 \Big/ \sqrt{|\boldsymbol{\alpha}'|^2 + \varepsilon}\right\} \tag{27}$$

$$\phi(\boldsymbol{\alpha}')^{-2} = \text{diag}\left\{\exp\left[-j2\phi(\boldsymbol{\alpha}')\right]\right\} \tag{28}$$

$\mathbf{I}$ is the identity matrix and ε is a small constant to avoid singularity when $\left|\boldsymbol{\alpha}'\right|$ approaches zero.

Examining the gradient expression of (25), the term $\mathbf{H}(\boldsymbol{\alpha}')$ resembles a "coefficient" matrix multiplying $\boldsymbol{\alpha}'$ [3]. As a result, we use $\mathbf{H}(\boldsymbol{\alpha}')$ as an approximation to the Hessian. Note that this Hessian approximation depends on $\boldsymbol{\alpha}'$ itself. We use this approximate Hessian in the following quasi-Newton iteration. Then $\boldsymbol{\alpha}'$ can be obtained as

$$\boldsymbol{\alpha}'^{(n+1)} = \boldsymbol{\alpha}'^{(n)} - \gamma_1 \left[\mathbf{H}(\boldsymbol{\alpha}'^{(n)})\right]^{-1} \nabla \boldsymbol{\alpha}'^{(n)} \tag{29}$$

where γ_1 is the scale for the step length.

To solve step 2 of Algorithm 2, the constrained optimization problem of equation (22) can be replaced with the following unconstrained problem

$$\min_{\boldsymbol{\beta}} \|\mathbf{s} - \mathbf{AB}\boldsymbol{\beta}\|_2 + \lambda_3 \sum_{i=1}^{PQ} \left(\left|\boldsymbol{\beta}_i\right| - 1\right)^2 \tag{30}$$

where λ_3 is the regularization parameter. Equation (30) can be rewritten as

$$\min_{\boldsymbol{\beta}} \|\mathbf{s} - \mathbf{AB}\boldsymbol{\beta}\|_2 + \lambda_3 \|\boldsymbol{\beta}\|_2^2 - 2\lambda_3 \|\boldsymbol{\beta}\|_1 \tag{31}$$

The gradient of the above cost function is

$$\nabla \boldsymbol{\beta} = 2(\mathbf{AB})^H(\mathbf{AB})\beta - 2(\mathbf{AB})^H\mathbf{s} + 2\lambda_3\boldsymbol{\beta} - 2\lambda_3\varphi(\boldsymbol{\beta}) \tag{32}$$

where $\phi(\boldsymbol{\beta}) = \exp[j\varphi(\boldsymbol{\beta})]$, $\varphi(\boldsymbol{\beta})$ is the phase of $\boldsymbol{\beta}$.

Again, equation (31) can be solved by quasi-Newton algorithms, as that the gradient is provided in equation (32). Here we also use the previously mentioned idea to determine the Hessian matrix. Equation (32) can be rewritten as

$$\nabla \boldsymbol{\beta} = \mathbf{H}(\boldsymbol{\beta})\boldsymbol{\beta} - 2(\mathbf{AB})^H\mathbf{s} \tag{33}$$

where

$$\mathbf{H}(\boldsymbol{\beta}) = 2(\mathbf{AB})^H(\mathbf{AB}) + 2\lambda_3\mathbf{I} - 2\lambda_3\boldsymbol{\Psi}(\beta) \tag{34}$$

$$\boldsymbol{\Psi}(\boldsymbol{\beta}) = \text{diag}\left\{1 \Big/ \sqrt{|\boldsymbol{\beta}|^2 + \varepsilon}\right\} \tag{35}$$

where ε is a small constant to avoid singularity when $|\boldsymbol{\beta}|$ tends to zero.

Given that the Hessian matrix is approximated as $\mathbf{H}(\boldsymbol{\beta})$, then $\boldsymbol{\beta}$ can be obtained by the following quasi-Newton iteration as

$$\boldsymbol{\beta}^{(n+1)} = \boldsymbol{\beta}^{(n)} - \gamma_2 \left[\mathbf{H}(\boldsymbol{\beta}^{(n)})\right]^{-1} \nabla \boldsymbol{\beta}^{(n)} \tag{36}$$

where γ_2 is the scale for the step length.

E. COMPUTATIONAL COMPLEXITY AND PARAMETERS ANALYSIS

As mentioned above, step 1 and step 2 of the proposed algorithm are solved by the quasi-Newton algorithm with novel Hessian matrices. In step 1 of the proposed algorithm, the size of $\boldsymbol{\Phi}'$ is $PQ \times K$ ($K = K_1K_2$), the size of $\mathbf{AP\Phi}'$ is also $PQ \times K$ and the size of $\boldsymbol{\alpha}'$ is $K \times 1$. In step 1 of the existing algorithm, the size of $\boldsymbol{\Phi}$ is $PQ \times PQ$, the size of $\mathbf{AP\Phi}$ is also $PQ \times PQ$ and the size of $\boldsymbol{\alpha}$ is $PQ \times 1$. For step 1, the computational complexity of the proposed algorithm is $K/(PQ)$ of the existing algorithm, both for the gradient computation and Hessian update. For step 2, the computational complexity of the proposed algorithm is approximately the same as the existing algorithm. In the existing algorithm, the computational complexity of step 1 and step 2 are about the same. As mentioned above, $K/(PQ)$ can be significantly smaller than 1, so the total computational complexity of the proposed algorithm is approximately half of that for the existing algorithm for each iteration. Furthermore, it should be noted that, since the real-valued magnitude information and the coefficient distribution information are utilized in the proposed algorithm, the reconstruction error of the proposed algorithm decreases more quickly when the number of iterations increases. That is to say, to achieve the same precision, the number of iterations of the proposed algorithm will be smaller than for the existing algorithm. So, the total computational complexity of the proposed algorithm will be less than half of the existing algorithm. Meanwhile, the quality of the result of the proposed algorithm will also be better than the existing algorithm. Both simulation and real data results in Section V will show these benefits for the proposed algorithm.

In the proposed algorithm,λ_1, λ_2 and λ_3 are the regularization parameters, which specify the strength of the constraining terms into the solution. The selection of λ_1, λ_2 and λ_3 involves a trade-off between relying on data or on the prior information [44]. For example, in equation (23), smaller values of λ_1 and λ_2 usually produce sparser magnitude. Thus, in general if we have enough information of the scene, such that the magnitude of the scene is very sparse in the DCT bases, smaller values of λ_1 and λ_2 will produce better results. There also has trade-off between the reconstruction precision of the magnitude and the phase. In equation (30), a larger value of λ_3 will produce an estimate of $\boldsymbol{\beta}$ with $\left|\boldsymbol{\beta}_i\right|$ closer to 1, but may lead to larger error in the data, which will influence the magnitude reconstruction. So the choice of the regularization parameters should be carefully considered according to the practical situations and requirements.

V. SIMULATION AND REAL DATA RESULTS

In order to demonstrate the superiority of the proposed algorithm, simulation and real data results are presented. The first simulation is for 1D imaging and the second simulation is for 2D SAR imaging. Some results of real data from an airborne SAR system are also presented.

As shown in Section IV-E, the choice of the regularization parameters is very important in the proposed algorithm. Since we are usually more interested in the magnitude of the obtained image for single channel SAR systems, we set relatively small values for λ_3 in this paper. The selection of the regularization parameters is also related to the noise level in the data [48]. Considering the above guidelines, we use $\lambda_1 = 1000$, $\lambda_2 = 100$ and $\lambda_3 = 0.001$ for the 1D and 2D simulation. $\lambda_1 = 100$, $\lambda_2 = 100$ and $\lambda_3 = 0.01$ are used for the real data processing. The scale for the step

TABLE 1. Simulation parameters for 1D imaging.

Bandwidth	256MHz
Sampling Rate	512MHz
Number of Samples	11264
Selected Samples	2048
Number of Range Points	1024
Number of Complete Bases	1024
Number of Reduced Bases	40

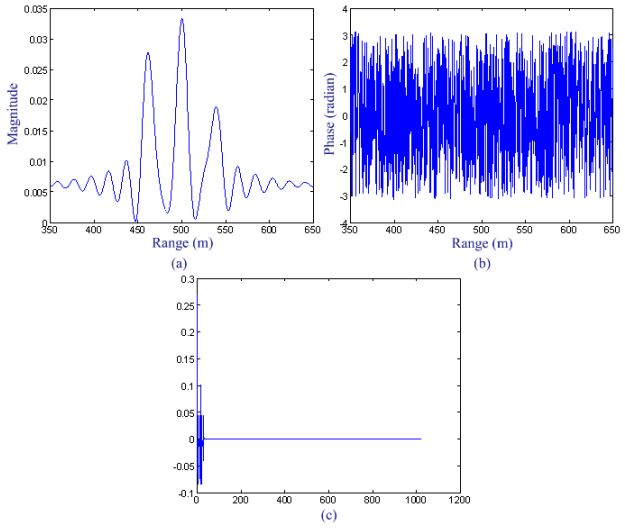

FIGURE 2. (a) Magnitude of the scene, (b) phase of the scene, (c) DCT result of the magnitude.

length γ_1 and γ_2 are set to 0.9. The small constant ε is set to 10^{-7}. The above values for the parameters are based on subjective and qualitative assessments of the obtained results. There are also automatic parameter selection methods [49] developed for similar problems that could be a direction of research in future work.

A. SIMULATION FOR 1D IMAGING

In order to compare the proposed algorithm with traditional radar imaging algorithms, the full data which satisfies the Nyquist sampling theorem is generated firstly. Then only part of the samples is selected for the CS-based reconstruction. Gaussian noise is added in the data, the signal to noise ratio (SNR) is 20 dB. The simulation parameters are shown in Table 1.

Fig. 2 (a) shows the magnitude of the scene and Fig. 2 (b) shows the phase of the scene. It can be seen that magnitude of the scene has a smooth shape but the phase is random. Fig. 2 (c) shows the DCT result of the magnitude. It can be seen that the coefficients are sparse and concentrated at low frequencies.

Fig. 3 (a) shows the result of traditional matched filtering (equation (6)) using the full data. It can be seen that although the scene has a smooth magnitude, the result has obvious fluctuations. Such phenomena reflect the reality that even in a SAR image of smooth terrain, there will exist speckle noise.

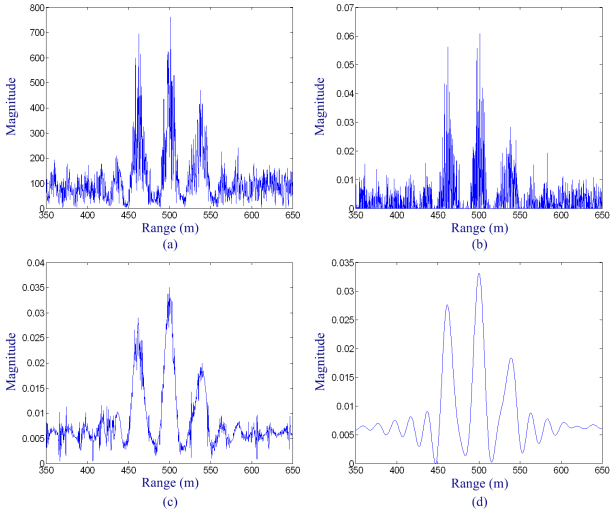

FIGURE 3. Reconstruction results, (a) matched filtering (full data), (b) CS-based algorithm without sparse representation, (c) existing magnitude sparsity-driven algorithm, (d) proposed algorithm.

Fig. 3 (b) shows the result of CS-based reconstruction without sparse representation (equation (7)), using 2048 samples. The reconstruction algorithm is SPGL1 [48]. Since the scene is not originally sparse, the reconstruction is inaccurate.

Fig. 3 (c) shows the result of the existing magnitude sparsity-driven reconstruction (Algorithm 1) using only 2048 samples. The complete DCT bases are used for sparse representation of the magnitude. It can be seen that the result contains much less noise fluctuation than the traditional matched filtering result.

Fig. 3 (d) shows the result of the proposed algorithm (Algorithm 2) using only 2048 samples. Only 40 DCT bases are used for sparse representation of the magnitude. The real-valued information of the magnitude is also exploited. It can be seen that the result has even less noise fluctuation than the existing magnitude sparsity-driven reconstruction. This implies that the proposed algorithm is superior to the existing algorithm in Fig. 3 (c).

Fig.4 shows the mean square error (MSE) of the reconstructed magnitude of the scene. It can be seen that since more *a priori* knowledge is used, the proposed algorithm has a smaller MSE than the existing magnitude sparsity-driven algorithm. The MSE of the proposed algorithm also decreases more quickly when the number of iterations increase. So, to achieve the same precision, the proposed algorithm requires fewer iterations. This can reduce the computational cost.

In this example, both the existing magnitude sparsity-driven algorithm and the proposed algorithm are implemented by non-optimized codes and run on the same computer. To compare the computational complexity, both the existing algorithm and the proposed algorithm have 20 iterations. The running time of the existing magnitude sparsity-driven algorithm is 1518s, the running time of the proposed algorithm is 834s. It can be seen that for the same

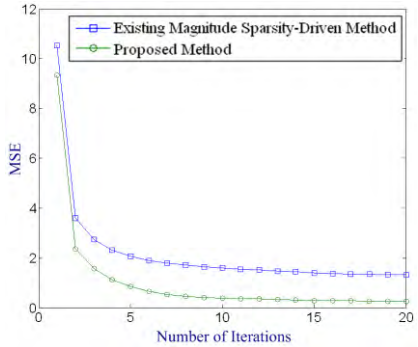

FIGURE 4. MSE comparison between existing magnitude sparsity-driven algorithm and the proposed algorithm.

TABLE 2. Simulation parameters for 2D imaging.

Center Frequency	10GHz
Bandwidth	512MHz
Number of Range Samples	2048
Number of Azimuth Samples	512
Selected Range Samples	64
Selected Azimuth Samples	64
Number of Range Points	64
Number of Azimuth Points	64
Number of Complete Bases	4096 (64×64)
Number of Reduced Bases	256 (16×16)

number of iterations, the proposed algorithm is about twice as fast as the existing algorithm. Considering that the MSE the proposed algorithm decreases more quickly than the existing algorithm, to achieve a same precision, the running time of the proposed algorithm will be less than half of the existing algorithm.

B. SIMULATION FOR 2D IMAGING

In this subsection, a 2D SAR imaging scenario is simulated. The simulation parameters are shown in Table 2. There are two extended objects placed in the scene, one of which has a round shape and the other has a rectangle shape. The scatterers that consist of these two objects have random phases associated with them.

Fig. 5 (a) shows the magnitude of the scene. Fig. 5 (b) shows the phase of the scene, which is random in $[-\pi, \pi]$. Fig. 5 (c) shows the DCT result of the magnitude. It can be seen that as expected the coefficients are sparse and concentrated at low frequencies.

Fig. 6 (a) shows the result of traditional matched filtering (equation (6)) using the full data. The imaging algorithm is the backprojection algorithm. It can be seen that although the scene has a smooth shape, the imaging result has obvious speckle.

Fig. 6 (b) shows the result of CS-based reconstruction without sparse representation (equation (7)), using 64 range samples and 64 azimuth samples. The reconstruction

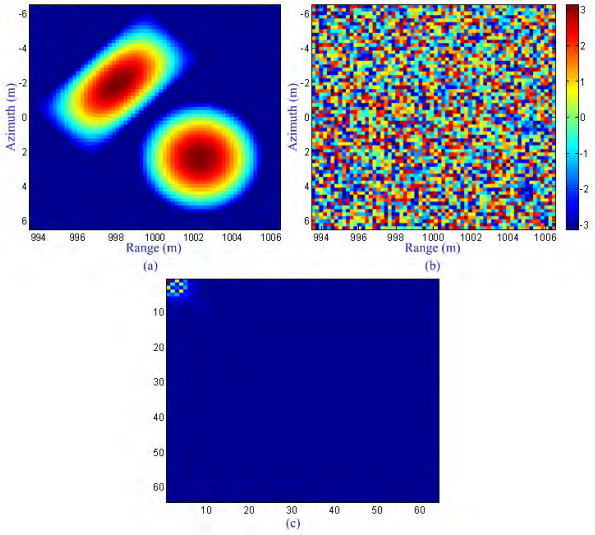

FIGURE 5. Scene of 2D imaging simulation. (a) Magnitude of the scene, (b) phase of the scene, (d) DCT result of the magnitude.

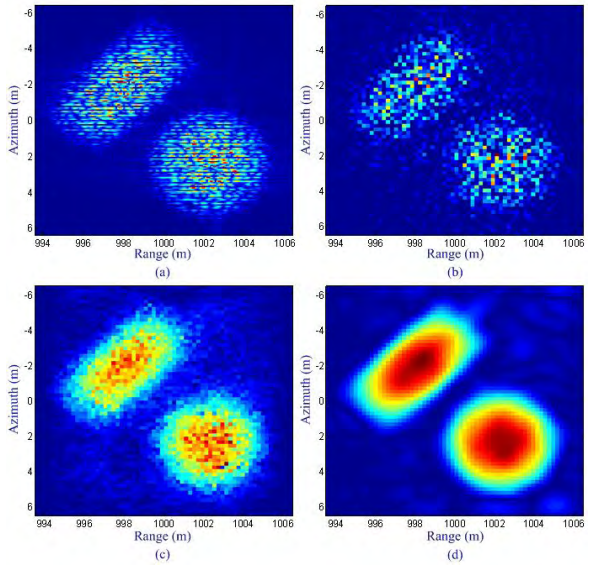

FIGURE 6. Reconstruction results, (a) matched filtering (full data), (b) CS-based algorithm without sparse representation, (c) existing magnitude sparsity-driven algorithm, (d) proposed algorithm.

algorithm is SPGL1. Since the scene is not originally sparse, the reconstruction is inaccurate.

Fig. 6 (c) shows the result of the existing magnitude sparsity-driven reconstruction (Algorithm 1) using 64 range samples and 64 azimuth samples. The complete DCT bases are used for sparse representation of the magnitude. It can be seen that the result has much less speckle than the traditional matched filtering result.

Fig. 6 (d) shows the result of the proposed algorithm (Algorithm 2) using 64 range samples and 64 azimuth samples. Only 256 (16 × 16) DCT bases are used for sparse representation of the magnitude. It can be seen that the result has less speckle than the existing magnitude sparsity-driven

FIGURE 7. Airborne SAR system, (a) antenna pod, (b) radar hardware system.

TABLE 3. Parameters of data 1.

Number of Azimuth Samples (Full Data)	2048
Number of Range Samples (Full Data)	2540
Selected Azimuth Samples	180
Selected Range Samples	90
Number of Azimuth Points	180
Number of Range Points	90
Number of Complete Bases	16200 (180×90)
Number of Reduced Bases	4050 (90×45)

reconstruction. This implies that the proposed algorithm is superior to the existing algorithm.

For 12 iterations, the running time of the existing magnitude sparsity-driven algorithm is 2892s, and the running time of the proposed algorithm is 1558s.

C. REAL DATA RESULTS

In this subsection, real data results will be presented. The raw data is acquired by an airborne SAR system. Fig. 7 shows the radar system. Fig. 7 (a) shows the antenna pod and Fig. 7 (b) shows the radar hardware system. The center frequency of the radar is 15GHz (Ku band), and the chirp signal bandwidth is 200MHz. The sampling rate is 250MHz. The velocity of the airplane is 105m/s and the pulse repetition frequency (PRF) is 500Hz. The original full data is under-sampled for the CS-based reconstruction. Three scenes are selected to demonstrate the effectiveness of the proposed algorithm.

Data 1 contains a scene of a farmland, in which there are crops. There is also some cleared land in the farmland scene. The reflectivity from the crops is different from that of the cleared land. The reconstruction parameters for Data 1 are shown in Table 3.

Fig. 8 (a) shows the result of traditional matched filtering (equation (6)) using the full data. The imaging algorithm is the backprojection algorithm. We can see the shape of the cleared land in the farmland. The crop lines are also visible in the image. However, there is significant speckle noise in the image, which degrades the quality of the image.

Fig. 8 (b) shows the result of CS-based reconstruction without sparse representation (equation (7)), using 180 azimuth samples and 90 range samples. The reconstruction algorithm is SPGL1. Since the scene is not originally sparse, the reconstruction is inaccurate.

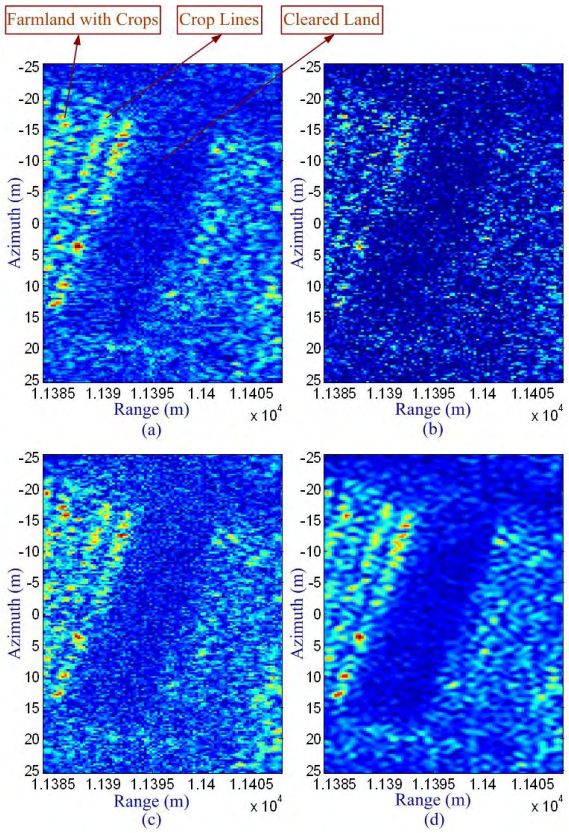

FIGURE 8. Reconstruction results of Data 1. (a) matched filtering (full data), (b) CS-based algorithm without sparse representation, (c) existing magnitude sparsity-driven algorithm, (d) proposed algorithm.

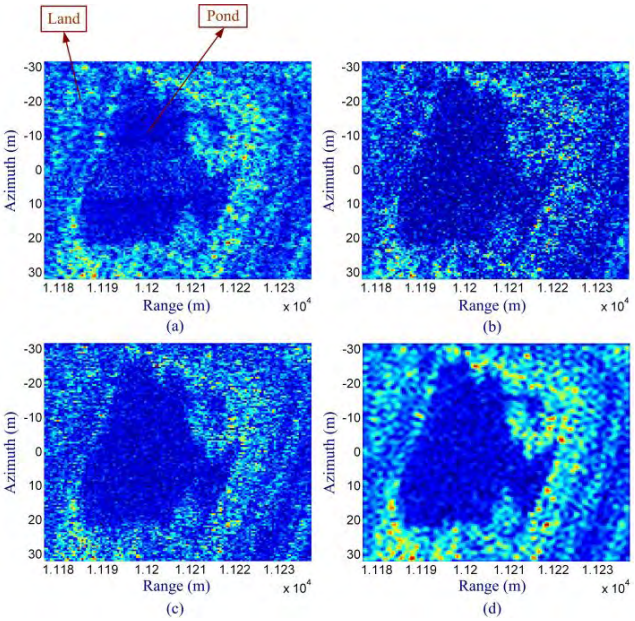

FIGURE 9. Reconstruction results of Data 2. (a) matched filtering (full data), (b) CS-based algorithm without sparse representation, (c) existing magnitude sparsity-driven algorithm, (d) proposed algorithm.

Fig. 8 (c) shows the result of the existing magnitude sparsity-driven reconstruction (Algorithm 1), using 180 azimuth samples and 90 range samples. The complete

TABLE 4. Parameters of data 2.

Number of Azimuth Samples (Full Data)	2048
Number of Range Samples (Full Data)	2600
Selected Azimuth Samples	128
Selected Range Samples	128
Number of Azimuth Points	128
Number of Range Points	128
Number of Complete Bases	16384(128×128)
Number of Reduced Bases	4096 (64×64)

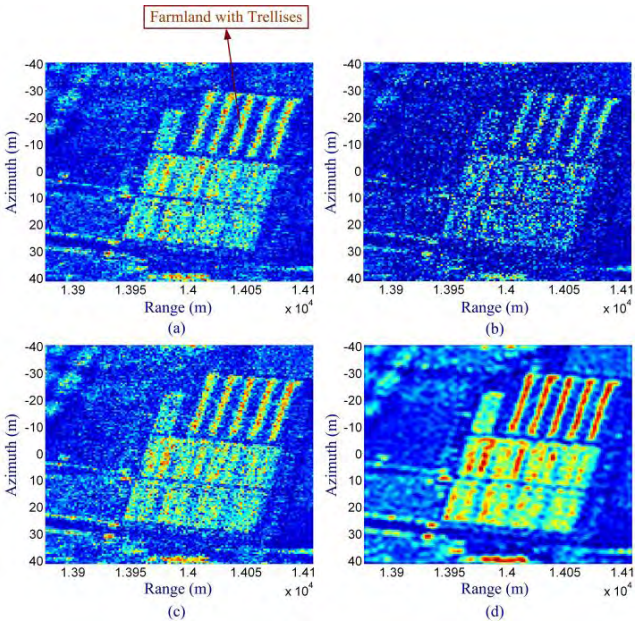

FIGURE 10. Reconstruction results of Data 3. (a) matched filtering (full data), (b) CS-based algorithm without sparse representation, (c) existing magnitude sparsity-driven algorithm, (d) proposed algorithm.

DCT bases are used for sparse representation of the magnitude. The farmland with crops and the cleared land are visible, but there is also significant speckle noise in the image.

Fig. 8 (d) shows the result of the proposed algorithm (Algorithm 2) using 180 azimuth samples and 90 range samples. Only 4050 (90 × 45) DCT bases are used for sparse representation of the magnitude. It can be seen that the image has less speckle than the existing magnitude sparsity-driven algorithm and the matched filtering algorithm. This implies that the proposed algorithm has superior performance compared to the existing algorithms.

In this example, due to the limitation of the computer memory, the selected signal samples are far fewer than the full samples. If the number of the selected samples increases, the proposed algorithm can achieve higher performance.

Data 2 contains a scene with a pond. The reflectivity from the water region of the pond is very low. The reconstruction parameters for Data 2 are shown in Table 4. The reconstruction results of Data 2 are shown in Fig. 9. Data 3 contains a scene of farmland with trellises. The reflectivity from the trellises is very strong. The reconstruction parameters for Data 3 are shown in Table 5. The reconstruction results of Data 3 are shown in Fig. 10. From the results of Data 2 and Data 3, it can be seen that the proposed algorithm can produce image with less speckle and clearer edge of different regions than the previous algorithms.

TABLE 5. Parameters of data 3.

Number of Azimuth Samples (Full Data)	2048
Number of Range Samples (Full Data)	2884
Selected Azimuth Samples	128
Selected Range Samples	128
Number of Azimuth Points	128
Number of Range Points	128
Number of Complete Bases	16384(128×128)
Number of Reduced Bases	4096 (64×64)

VI. CONCLUSIONS

In this paper, an improved magnitude sparsity-driven and CS-based SAR imaging algorithm is proposed. It can effectively handle the potentially random phase of the SAR scene. Besides the sparsity in the magnitude, the real-valued information of the magnitude and the coefficient distribution of the sparse representation are also utilized in the proposed algorithm. A novel gradient-based algorithm is developed to solve the optimization problem effectively. Since more *a priori* knowledge is utilized in the proposed algorithm, it can reduce the computational complexity and improve the reconstruction precision. Compared to the existing magnitude sparsity-driven algorithm, the proposed algorithm can obtain higher quality images with about half running time.

The proposed algorithm is a sparsity-driven and regularization-based imaging algorithm. It maintains the advantages of such type of algorithms, including increased image quality and robustness to limitations in data quantity. The latter is the aim of compressed sensing. So compressed sensing is a special case of the algorithm proposed in this paper, which aims to reduce the number of data samples.

REFERENCES

[1] I. G. Cumming and F. H. Wong, *Digital Processing of Synthetic Aperture Radar Data: Algorithms and Implementation*. Boston, MA, USA: Artech House, 2005.

[2] J. H. G. Ender, "On compressive sensing applied to radar," *Signal Process.*, vol. 90, no. 5, pp. 1402–1414, May 2010.

[3] M. Çetin and W. C. Karl, "Feature-enhanced synthetic aperture radar image formation based on nonquadratic regularization," *IEEE Trans. Image Process.*, vol. 10, no. 4, pp. 623–631, Apr. 2001.

[4] L. Li *et al.*, "A survey on the low-dimensional-model-based electromagnetic imaging," *Found. Trends Signal Process.*, vol. 12, no. 2, pp. 107–199, Jan. 2018.

[5] L. Wang, L. Li, J. Ding, and T. Cui, "A fast patches-based imaging algorithm for 3-D multistatic imaging," *IEEE Geosci. Remote Sens. Lett.*, vol. 14, no. 6, pp. 941–945, Jun. 2017.

[6] G. Dong, G. Kuang, N. Wang, and W. Wang, "Classification via sparse representation of steerable wavelet frames on Grassmann manifold: Application to target recognition in SAR image," *IEEE Trans. Image Process.*, vol. 26, no. 6, pp. 2892–2904, Jun. 2017.

[7] D. L. Donoho, "Compressed sensing," *IEEE Trans. Inf. Theory*, vol. 52, no. 4, pp. 1289–1306, Apr. 2006.

[8] E. J. Candès, J. Romberg, and T. Tao, "Robust uncertainty principles: Exact signal reconstruction from highly incomplete frequency information," *IEEE Trans. Inf. Theory*, vol. 52, no. 2, pp. 489–509, Feb. 2006.
[9] D. L. Donoho, M. Elad, and V. N. Temlyakov, "Stable recovery of sparse overcomplete representations in the presence of noise," *IEEE Trans. Inf. Theory*, vol. 52, no. 1, pp. 6–18, Jan. 2006.
[10] E. J. Candès and T. Tao, "Near-optimal signal recovery from random projections: Universal encoding strategies?" *IEEE Trans. Inf. Theory*, vol. 52, no. 12, pp. 5406–5425, Dec. 2006.
[11] R. G. Baraniuk, "Compressive sensing," *IEEE Signal Process. Mag.*, vol. 24, no. 4, pp. 118–121, Jul. 2007.
[12] J. Romberg, "Imaging via compressive sampling," *IEEE Signal Process. Mag.*, vol. 25, no. 2, pp. 14–20, Mar. 2008.
[13] R. G. Baraniuk and P. Steeghs, "Compressive radar imaging," in *Proc. IEEE Radar Conf.*, Boston, MA, USA, Apr. 2007, pp. 128–133.
[14] L. C. Potter, E. Ertin, J. T. Parker, and M. Cetin, "Sparsity and compressed sensing in radar imaging," *Proc. IEEE*, vol. 98, no. 6, pp. 1006–1020, Jun. 2010.
[15] M. Cętin *et al.*, "Sparsity-driven synthetic aperture radar imaging: Reconstruction, autofocusing, moving targets, and compressed sensing," *IEEE Signal Process. Mag.*, vol. 31, no. 4, pp. 27–40, Jul. 2014.
[16] V. M. Patel, G. R. Easley, D. M. Healy, Jr., and R. Chellappa, "Compressed synthetic aperture radar," *IEEE J. Sel. Topics Signal Process.*, vol. 4, no. 2, pp. 244–254, Apr. 2010.
[17] M. T. Alonso, P. Lopez-Dekker, and J. Mallorqui, "A novel strategy for radar imaging based on compressive sensing," *IEEE Trans. Geosci. Remote Sens.*, vol. 48, no. 12, pp. 4285–4295, Dec. 2010.
[18] K. R. Varshney, M. Çetin, J. W. Fisher, and A. S. Willsky, "Sparse representation in structured dictionaries with application to synthetic aperture radar," *IEEE Trans. Signal Process.*, vol. 56, no. 8, pp. 3548–3561, Aug. 2008.
[19] N. Ö. Onhon and M. Cetin, "A sparsity-driven approach for joint SAR imaging and phase error correction," *IEEE Trans. Image Process.*, vol. 21, no. 4, pp. 2075–2088, Apr. 2012.
[20] L. Yang, J. Zhou, L. Hu, and H. Xiao, "A perturbation-based approach for compressed sensing radar imaging," *IEEE Antennas Wireless Propag. Lett.*, vol. 16, pp. 87–90, 2017.
[21] Y. G. Lin, B. C. Zhang, W. Hong, and Y. R. Wu, "Along-track interferometric SAR imaging based on distributed compressed sensing," *Electron. Lett.*, vol. 46, no. 12, pp. 858–860 Jun. 2010.
[22] L. Prünte, "Compressed sensing for joint ground imaging and target indication with airborne radar," in *Proc. 4th Workshop Signal Process, Adapt. Sparse Structured Represent.*, Edinburgh, U.K., Jun. 2011, p. 22.
[23] Q. Wu, M. Xing, C. Qiu, B. Liu, Z. Bao, and T.-S. Yeo, "Motion parameter estimation in the SAR system with low PRF sampling," *IEEE Geosci. Remote Sens. Lett.*, vol. 7, no. 3, pp. 450–454, Jul. 2010.
[24] I. Stojanovic and W. C. Karl, "Imaging of moving targets with multistatic SAR using an overcomplete dictionary," *IEEE J. Sel. Topics Signal Process.*, vol. 4, no. 1, pp. 164–176, Feb. 2010.
[25] N. Ö. Önhon and M. Çetin, "SAR moving target imaging in a sparsity-driven framework," *Proc. SPIE*, vol. 8138, Sep. 2011, Art. no. 813806. doi:10.1117/12.893581.
[26] X. X. Zhu, N. Ge, and M. Shahzad, "Joint sparsity in SAR tomography for urban mapping," *IEEE J. Sel. Topics Signal Process.*, vol. 9, no. 8, pp. 1498–1509, Dec. 2015.
[27] X. X. Zhu and R. Bamler, "Super-resolution power and robustness of compressive sensing for spectral estimation with application to spaceborne tomographic SAR," *IEEE Trans. Geosci. Remote Sens.*, vol. 50, no. 1, pp. 247–258, Jan. 2012.
[28] X. X. Zhu and R. Bamler, "Demonstration of super-resolution for tomographic SAR imaging in urban environment," *IEEE Trans. Geosci. Remote Sens.*, vol. 50, no. 8, pp. 3150–3157, Aug. 2012.
[29] A. Budillon, A. Evangelista, and G. Schirinzi, "Three-dimensional SAR focusing from multipass signals using compressive sampling," *IEEE Trans. Geosci. Remote Sens.*, vol. 49, no. 1, pp. 488–499, Jan. 2011.
[30] S. Xilong, Y. Anxi, D. Zhen, and L. Diannong, "Three-dimensional SAR focusing via compressive sensing: The case study of angel stadium," *IEEE Geosci. Remote Sens. Lett.*, vol. 9, no. 4, pp. 759–763, Jul. 2012.
[31] E. Aguilera, M. Nannini, and A. Reigber, "Multisignal compressed sensing for polarimetric SAR tomography," *IEEE Geosci. Remote Sens. Lett.*, vol. 9, no. 5, pp. 871–875, Sep. 2012.
[32] H. Kajbaf, "Compressed sensing for 3D microwave imaging systems," Ph.D. dissertation, Dept. Elect. Comput. Eng., Missouri Univ. Sci. Technol., Rolla, MO, USA, 2012.
[33] S. Zhang, G. Dong, and G. Kuang, "Superresolution downward-looking linear array three-dimensional SAR imaging based on two-dimensional compressive sensing," *IEEE J. Sel. Topics Appl. Earth Observ. Remote Sens.*, vol. 9, no. 6, pp. 2184–2196, Jun. 2016.
[34] H. Tian and D. Li, "Sparse flight array SAR downward-looking 3-D imaging based on compressed sensing," *IEEE Geosci. Remote Sens. Lett.*, vol. 13, no. 10, pp. 1395–1399, Oct. 2016.
[35] L. Zhang, Z.-J. Qiao, M. Xing, Y. Li, and Z. Bao, "High-resolution ISAR imaging with sparse stepped-frequency waveforms," *IEEE Trans. Geosci. Remote Sens.*, vol. 49, no. 11, pp. 4630–4651, Nov. 2011.
[36] H. Wang, Y. Quan, M. Xing, and S. Zhang, "ISAR imaging via sparse probing frequencies," *IEEE Geosci. Remote Sens. Lett.*, vol. 8, no. 3, pp. 451–455, May 2011.
[37] X. Du, C. Duan, and W. Hu, "Sparse representation based autofocusing technique for ISAR images," *IEEE Trans. Geosci. Remote Sens.*, vol. 51, no. 3, pp. 1826–1835, Mar. 2013.
[38] A. B. Suksmono, E. Bharata, A. A. Lestari, A. G. Yarovoy, and L. P. Ligthart, "Compressive stepped-frequency continuous-wave ground-penetrating radar," *IEEE Geosci. Remote Sens. Lett.*, vol. 7, no. 4, pp. 665–669, Oct. 2010.
[39] A. C. Gurbuz, J. H. McClellan, and W. R. Scott, "A compressive sensing data acquisition and imaging method for stepped frequency GPRs," *IEEE Trans. Signal Process.*, vol. 57, no. 7, pp. 2640–2650, Jul. 2009.
[40] M. A. C. Tuncer and A. C. Gurbuz, "Ground reflection removal in compressive sensing ground penetrating radars," *IEEE Geosci. Remote Sens. Lett.*, vol. 9, no. 1, pp. 23–27, Jan. 2012.
[41] M. F. Duarte *et al.*, "Single-pixel imaging via compressive sampling," *IEEE Signal Process. Mag.*, vol. 25, no. 2, pp. 83–91, Mar. 2008.
[42] M. Çetin, W. C. Karl, and A. S. Willsky, "Feature-preserving regularization method for complex-valued inverse problems with application to coherent imaging," *Opt. Eng.*, vol. 45, no. 1, p. 017003, Jan. 2006.
[43] M. Çetin, N. Ö. Önhon, and S. Samadi, "Handling phase in sparse reconstruction for SAR: imaging, autofocusing, and moving targets," in *Proc. EUSAR*, Nuremberg, Germany, Apr. 2012, pp. 207–210.
[44] S. Samadi, M. Çetin, and M. A. Masnadi-Shirazi, "Sparse representation-based synthetic aperture radar imaging," *IET Radar, Sonar Navigat.*, vol. 5, no. 2, pp. 182–193, Feb. 2011.
[45] J. Yang, J. Thompson, X. Huang, T. Jin, and Z. Zhou, "Segmented reconstruction for compressed sensing SAR imaging," *IEEE Trans. Geosci. Remote Sens.*, vol. 51, no. 7, pp. 4214–4225, Jul. 2013.
[46] S. S. Chen, D. L. Donoho, and M. A. Saunders, "Atomic decomposition by basis pursuit," *SIAM J. Sci. Comput.*, vol. 20, no. 1, pp. 33–61, 1999.
[47] J. A. Tropp and A. C. Gilbert, "Signal recovery from random measurements via orthogonal matching pursuit," *IEEE Trans. Inf. Theory*, vol. 53, no. 12, pp. 4655–4666, Dec. 2007.
[48] E. van den Berg and M. P. Friedlander, "Probing the Pareto frontier for basis pursuit solutions," *SIAM J. Sci. Comput.*, vol. 31, no. 2, pp. 890–912, 2008.
[49] O. Batu and M. Çetin, "Parameter selection in sparsity-driven SAR imaging," *IEEE Trans. Aerosp. Electron. Syst.*, vol. 47, no. 4, pp. 3040–3050, Oct. 2011.

JUNGANG YANG (S'10–M'13) received the B.S. degree in electronic engineering and the M.S. and Ph.D. degrees in information and communication engineering from the National University of Defense Technology, Changsha, China, in 2007, 2008, and 2013, respectively.

From 2010 to 2011, he was a Visiting Ph.D. Student with The University of Edinburgh, Edinburgh, U.K. He is currently an Associate Professor with the National University of Defense Technology. His research interests include radar imaging, computational imaging, compressed sensing, sparse representation, and image processing.

Dr. Yang was a recipient of the New Academic of Chinese Ministry of Education Award, in 2012, the Youth Innovation Award, the Youth Outstanding Talent of National University of Defense Technology, in 2016, the Excellent Doctoral Dissertation of Hunan Province Award, in 2016, and the Excellent Doctoral Dissertation of China Education Society of Electronics Award, in 2017. He was sponsored by the Innovation Project of National University of Defense Technology for Excellent Graduate Student, in 2012.

TIAN JIN (S'07–M'08) received the B.S., M.Sc., and Ph.D. degrees in information and communication engineering from the National University of Defense Technology, Changsha, China, in 2002, 2003, and 2007, respectively, where he is currently a Professor.

His research interests include synthetic aperture radar systems and ground-penetrating radar.

Dr. Jin received the National Excellent Doctoral Dissertation of China Award for his Ph.D. dissertation, in 2009.

XIAOTAO HUANG (M'07) received the B.S. and Ph.D. degrees in information and communication engineering from the National University of Defense Technology, Changsha, China, in 1994 and 1999, respectively, where he is currently a Professor.

His research interests include synthetic aperture radar systems and array signal processing.

Dr. Huang is a Senior Member of the Chinese Institute of Electronics.